# Journal of Materials Chemistry A

Accepted Manuscript


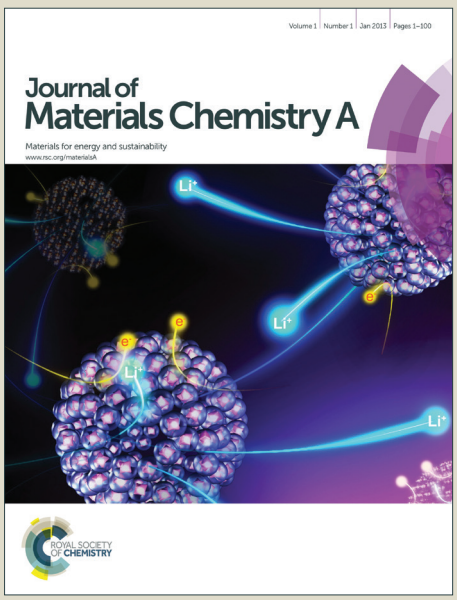





ROYAL SOCIETY OF CHEMISTRY

www.rsc.org/materialsA

Journal Name

RSCPublishing

ARTICLE

# Towards the endothermic dehydrogenation of nanoconfined magnesium borohydride ammoniate†

Cite this: DOI: 10.1039/xoxxoooooox

Yanjing Yang,[a,b] Yongfeng Liu,*[a] You Li,[a] Xin Zhang,[a] Mingxia Gao,[a] Hongge Pan*[a]

Received ooth January 2012,
Accepted ooth January 2012

DOI: 10.1039/xoxxoooooox

www.rsc.org/

The utilization of metal borohydride ammoniates as practical hydrogen storage materials is hindered by their unfavorable exothermic dehydrogenation thermodynamics. Here, we report a first successful attempt to tailor the dehydrogenation thermodynamics of magnesium borohydride hexaammoniate ($Mg(BH_4)_2{\cdot}6NH_3$) through nanoconfinement into microporous activated carbon (AC). The onset temperature for hydrogen release from the nanoconfined $Mg(BH_4)_2{\cdot}6NH_3$ is dramatically decreased to approximate 40 ºC, and more encouragingly, hydrogen desorption is endothermic in nature. The relationship between pore size and dehydrogenation behavior is established, and the critical pore size for the endothermic dehydrogenation of the nanoconfined $Mg(BH_4)_2{\cdot}6NH_3$ is found to be less than 4 nm. The nanoconfinement effect of carbon scaffolds is believed to be the primary reason for the change in the dehydrogenation pathway caused by incorporating $Mg(BH_4)_2{\cdot}6NH3$ into microporous activated carbon. This finding opens up the possibility to achieve reversible hydrogen storage in metal borohydride ammoniates.

## 1 Introduction

Hydrogen is a clean, highly abundant energy carrier with the highest energy density of all known chemical fuels (120-142 MJ $kg^{-1}$), thus making it an attractive candidate for future energy systems.[1] However, large-scale utilization of hydrogen is currently hindered by the inadequate storage properties of the present hydrogen-storage technologies. In the past several decades, the research focus has been solid-state hydrogen storage materials due to their much higher gravimetric and volumetric hydrogen capacities as well as their safer operating conditions compared with traditional pressurized gas and liquefied hydrogen storage.[2,3]

Metal borohydrides, including $LiBH_4$, $Mg(BH_4)_2$ and $Ca(BH_4)_2$, which have high hydrogen capacities, are promising solid-state hydrogen storage materials.[4] Among these materials, $Mg(BH_4)_2$ possesses a gravimetric hydrogen density of 14.9 wt% and a volumetric hydrogen density of 112 g $L^{-1}$ with a favorable desorption enthalpy of -38 kJ $mol^{-1}$ of $H_2$ at 25 ºC, meeting the target set by the U.S. Department of Energy (DOE).[5] Unfortunately, the high kinetic barrier of $Mg(BH_4)_2$ causes most of its dehydrogenation to occur at temperatures above 300 ºC, which is too high for practical applications.[6] Recently, it was found that creating a coexisting environment of hydric ($H^{\delta-}$) hydrogen atoms (Lewis base) and protonic ($H^{\delta+}$) hydrogen atoms (Lewis acid) could significantly improve the hydrogen storage properties of metal borohydrides.[7] According to this strategy, $Mg(BH_4)_2{\cdot}2NH_3$ was proposed to be a potentially promising material for hydrogen storage due to its high hydrogen capacity (~16.0 wt%) and low dehydrogenation temperature (~150 ºC).[8] Following this work, a series of borohydride ammoniates were designed and investigated as hydrogen storage materials, including $LiBH_4{\cdot}NH_3$, $Mg(BH_4)_2{\cdot}xNH_3$, $Ca(BH_4)_2{\cdot}2NH_3$, $Al(BH_4)_3{\cdot}6NH_3$, $Li_2Mg(BH_4)_4{\cdot}6NH_3$ and $Li_2Al(BH_4)_5{\cdot}6NH_3$ etc.[9-15] Among these compounds, the coordination of $NH_3$ to $M^{n+}$ (M: metal) allows protonic ($H^{\delta+}$) hydrogen atoms to coexist with hydric ($H^{\delta-}$) hydrogen atoms in the $[BH_4]^-$ anions. Thus, the local combination of the N-$H^{\delta+}$···$H^{\delta-}$-B dihydrogen bonds in metal borohydride ammoniates leads to hydrogen release at temperatures lower than those of the corresponding metal borohydrides. However, the limited reversibility for hydrogen storage in metal borohydride ammoniates prohibits their use in practical on-board applications. This is mainly due to the exothermic nature of their dehydrogenation processes, during which thermodynamically stable B-N compounds are formed.

Considerable efforts have been devoted to tailoring the thermodynamic properties for hydrogen storage in complex hydrides.[16-24] One encouraging approach is to introduce size effects in hydrides by incorporating them into inert nanoporous scaffolds, *viz.*, nanoconfinement or support, to prepare nanosized materials.[24-35] In 2005, a seminal work on the effects of nanoconfinement on the hydrogen storage properties of ammonia borane ($NH_3BH_3$) in an ordered mesoporous silica

scaffold (SBA-15) with a pore diameter of 7-8 nm was reported.[26] It was shown that nanoconfinement not only improved the hydrogen-release kinetics but also altered the reaction pathway and thermodynamic properties. Since this discovery, nanoconfinement has been extensively studied as an important and feasible approach to manipulate the thermodynamics and kinetics for hydrogen storage in complex hydride systems.[27-34] The reversibility of hydrogen release was impressively facilitated by nanoconfining the materials in a scaffold.[27,28] More interestingly, $NaAlH_4$ nanoconfined in porous carbon with 0.5-4-nm pores exhibited the isothermal behavior of a solid solution to a greater degree.[29] Further experiments on $LiBH_4$, $NaBH_4$, $Mg(BH_4)_2$ and $Li_3BN_2H_8$ largely confirm these results.[30-34] More encouragingly, Li *et al.* recently found that the dehydrogenation properties of $LiBH_4{\cdot}NH_3$ confined in nanoporous silicon dioxide were also significantly improved.[35] However, it has not dealt with the effect of nanoconfinement on the dehydrogenation thermodynamics of borohydride ammoniate.

In this work, we describe a first attempt to understand how the thermodynamic behaviors of borohydride ammoniates are influenced by particle size. $Mg(BH_4)_2{\cdot}6NH_3$ nanoparticles were formed by the in-situ ammoniation of magnesium borohydride dietherate $Mg(BH_4)_2{\cdot}2Et_2O$ confined in activated carbon (AC) and porous carbon (PC) with different pore sizes. Their dehydrogenation thermodynamics and kinetics were systematically studied. It was found that hydrogen desorption from $Mg(BH_4)_2{\cdot}6NH_3$ confined in porous scaffolds with a pore size of less than 4 nm was endothermic in nature, revealing its important potential for use in reversible hydrogen storage. To the best of our knowledge, this is the first report of metal borohydride ammonites undergoing endothermic processes upon thermal dehydrogenation, which is of great significance for the use of these materials in reversible hydrogen storage.

## 2 Experimental Section

All of the sample handling was performed in either a Schlenk apparatus or a glovebox (MBRAUN 200B) equipped with a circulation purifier to keep the concentration of $O_2$ and $H_2O$ below 1 ppm during operation.

### 2.1 Materials and Sample Preparation

The commercially available chemicals sodium borohydride ($NaBH_4$, 98%, Alfa Aesar) and magnesium chloride ($MgCl_2$, 99%, Alfa Aesar) were purchased and used as received. Anhydrous diethyl ether was obtained from Sinopharm Chemical and further dried with calcium hydride. Anhydrous ammonia ($NH_3$, 99%) was also used as received. Magnesium borohydride ($Mg(BH_4)_2$, 96%) was synthesized via a metathesis reaction between sodium borohydride and magnesium chloride in diethyl ether as described in our previous report.[36] Activated carbon (AC) with 2-nm pores was purchased from Nanjing XFNANO Materials Tech Co., Ltd, and pretreated at 400 ºC in a dynamic vacuum for 24 h to remove the adsorbed moisture. Nonporous graphite (synthetic, 99%) with a similar particle size to AC (Figure S1, ESI) was also obtained from Alfa Aesar and subjected to the same pretreatment procedure. Three porous carbons with average pore sizes of 4, 6 and 10 nm were purchased from Nanjing XFNANO Materials Tech Co., Ltd, and Sigma Aldrich and degased at 400 ºC for 24 h before use. The morphological characteristics of activated carbon and porous carbons were listed in Table S1 (ESI).

The bulk $Mg(BH_4)_2{\cdot}6NH_3$ was prepared through the reaction of magnesium borohydride dietherate ($Mg(BH_4)_2{\cdot}2Et_2O$) and ammonia gas ($NH_3$). Firstly, $Mg(BH_4)_2$ was dissolved in $Et_2O$ in a round-bottom flask. Next, the solution was magnetically stirred for 3 h and subjected to pumping to obtain the viscous $Mg(BH_4)_2{\cdot}2Et_2O$. Finally, anhydrous ammonia ($NH_3$) was introduced into the flask to react with $Mg(BH_4)_2{\cdot}2Et_2O$ to produce $Mg(BH_4)_2{\cdot}6NH_3$. The resulting product was identified to be $Mg(BH_4)_2{\cdot}6NH_3$ (Figure S2, ESI).[37]

The composites comprised of $Mg(BH_4)_2{\cdot}6NH_3$ and activated carbon, porous carbon and graphite (denoted as $Mg(BH_4)_2{\cdot}6NH_3$@AC, $Mg(BH_4)_2{\cdot}6NH_3$@PC and $Mg(BH_4)_2{\cdot}6NH_3$@graphite, respectively) were prepared by wetness impregnation associated with subsequent in-situ ammoniation. Typically, the mixtures of $Mg(BH_4)_2$ and the carbon scaffold (activated carbon, porous carbon and graphite) were first ground evenly with a mortar and pestle and then transferred to a 50-mL round-bottom flask, after which 30 mL of $Et_2O$ was added to the flask. The flask was subjected to magnetic stirring for 3 h at room temperature, and then the solvent $Et_2O$ was slowly pumped out at 0 ºC. To ensure the penetration of liquid magnesium borohydride dietherate into activated carbon, the residuals were further subjected to 0 ºC for 3 h. Next, the in-situ ammoniation process was carried out by slowly introducing anhydrous $NH_3$ into the flask. An operation temperature of 0 ºC and magnetic stirring were required in this process to prevent the temperature rise.

### 2.2 Property Evaluation

Temperature-programmed desorption (TPD) measurements were performed on a homemade apparatus coupled with online mass spectroscopy (MS, Hiden QIC-20). Approximately 40 mg of sample was loaded into a specially designed tube reactor that allows the purge argon to pass through upon heating. The temperature was gradually elevated from room temperature to 600 ºC at a rate of 2 ºC $min^{-1}$.

A Netzsch DSC 200 F3 thermal analyzer was employed to determine the heat flow of the as-prepared samples under a 50 mL $min^{-1}$ Ar flow. Thermogravimetric analysis (TG) was conducted on a Netzsch STA449F3 thermal analyzer. The sample was gradually heated from room temperature to 400 ºC.

The hydrogen storage properties were quantitatively evaluated with a homemade Sieverts-type apparatus. Approximately 150 mg of sample was loaded into a stainless-steel reactor in the glove box and then connected to the Sieverts-type apparatus. The sample was heated to the desired temperature at 2 ºC $min^{-1}$ (initially in vacuum) for

dehydrogenation and 1 ºC $min^{-1}$ (initial hydrogen pressure of 100 bar) for hydrogenation.

### 2.3 Structural and Morphologic Characterization

Phase identification was conducted using powder X-ray diffraction (XRD) on a Phillips X'Pert Pro X-ray diffractometer with Cu Kα radiation (λ=1.5418 Å) at 40 kV and 40 mA. Data were collected from 10º to 90º (2$\theta$) in increments of 0.02º at ambient temperature. The vibrational characteristics of the B-H and N-H bonds were determined by a Bruker Tensor 27 Fourier transform infrared (FTIR) spectrometer. FTIR spectra of all of the samples (as KBr pellets with a KBr-to-sample weight ratio of approximately 100:1) were acquired in the range of 4000 to 400 $cm^{-1}$, and transmission mode was adopted with a resolution of 4 $cm^{-1}$.

Scanning electron microscopy (SEM, Hitachi, S-4800) was used to characterize the powder morphology. The porosity analyses were conducted by $N_2$-physisorption at -196 ºC using an Autosorb-1-C instrument (Quantachrome, USA). The samples were loaded into the quartz sample tubes in the glovebox to prevent contamination from oxygen and moisture.

X-ray photoelectron spectroscopy (XPS) analyses were conducted on an ESCALAB 250 Xi XPS microprobe (Thermo Scientific, UK). The sample was prepared by sprinkling powder on a carbon tape attached to the sample holder in the glovebox. XPS spectra were recorded using monochromatic Al-Kα (1486.6 eV) X-ray sources under an ultimate pressure of $5\times10^{-10}$ mbar. All data were calibrated using the adventitious C 1s signal at 284.8 eV as a reference.

## 3 Results and Discussion

### 3.1 Structure and Morphology of Nanoconfined $Mg(BH_4)_2{\cdot}6NH_3$@AC

$Mg(BH_4)_2{\cdot}6NH_3$ was confined in the AC scaffold by wetness impregnation and subsequent in-situ ammoniation process, as schematically illustrated in Figure 1. The weight ratios of the starting materials of $Mg(BH_4)_2$ and AC were designed to be 1:1, 0.8:1, 0.6:1, 0.4:1 and 0.2:1. The resulting nanoconfinement products were described as 1:1 $Mg(BH_4)_2{\cdot}6NH_3$@AC, 0.8:1 $Mg(BH_4)_2{\cdot}6NH_3$@AC, 0.6:1 $Mg(BH_4)_2{\cdot}6NH_3$@AC, 0.4:1 $Mg(BH_4)_2{\cdot}6NH_3$@AC and 0.2:1 $Mg(BH_4)_2{\cdot}6NH_3$@AC, respectively. SEM observation revealed a mild increase in particle size for the resulting products with increasing AC contents. The 1:1 $Mg(BH_4)_2{\cdot}6NH_3$@AC sample exhibited a particle morphology similar to $Mg(BH_4)_2{\cdot}6NH_3$, while the morphology is more similar to that of AC for the 0.2:1 sample (Figure S3, ESI).

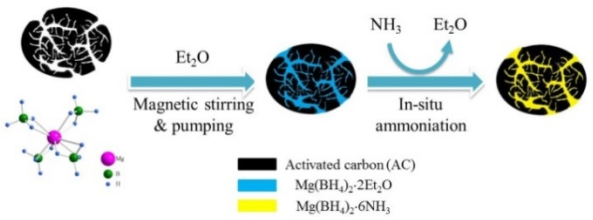


**Figure 1**. Schematic preparation procedure of the nanoconfined $Mg(BH_4)_2{\cdot}6NH_3$.

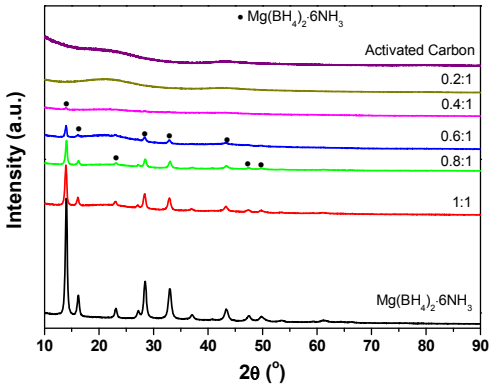


**Figure 2**. XRD patterns of the commercial AC, bulk $Mg(BH_4)_2{\cdot}6NH_3$ and $Mg(BH_4)_2{\cdot}6NH_3$@AC nanocomposites.

Figure 2 shows the XRD patterns of the as-prepared $Mg(BH_4)_2{\cdot}6NH_3$@AC nanocomposites. For comparison, the XRD data of the bulk $Mg(BH_4)_2{\cdot}6NH_3$ and AC are also presented in Figure 2. It is observed that the bulk $Mg(BH_4)_2{\cdot}6NH_3$ exhibits sharp diffraction peaks, indicating good crystallinity. Only two broad peaks, 2$\theta$ = 15-30º and 40-45º, were observed in the XRD profile of AC, representing its amorphous structure. For the nanoconfined samples, the characteristic reflections of $Mg(BH_4)_2{\cdot}6NH_3$ were distinctly weakened and even disappeared with increasing AC contents. In particular, only the typical two broad peaks of AC were discernable in the XRD pattern of the 0.2:1 $Mg(BH_4)_2{\cdot}6NH_3$@AC composite, with the absence of $Mg(BH_4)_2{\cdot}6NH_3$ peaks being due to the lower relative content of $Mg(BH_4)_2{\cdot}6NH_3$ and/or nanoconfinement effects. However, the diffraction peaks of $Mg(BH_4)_2{\cdot}6NH_3$ were unambiguously identified with considerable intensities in the XRD profile of the 0.2:1 $Mg(BH_4)_2{\cdot}6NH_3$@graphite composite in addition to those of graphite (Figure S4, ESI). This is mainly because the commercial graphite is a bulk material without porosity, preventing nanoconfinement for the $Mg(BH_4)_2{\cdot}6NH_3$@graphite composites. Accordingly, the disappearance of $Mg(BH_4)_2{\cdot}6NH_3$ in the XRD pattern of the 0.2:1 $Mg(BH_4)_2{\cdot}6NH_3$@AC composite can be attributed to the nanoconfinement effect. In other words, $Mg(BH_4)_2{\cdot}6NH_3$ should be confined in AC micropores for the 0.2:1 $Mg(BH_4)_2{\cdot}6NH_2$@AC composite. Such a conjecture was further proved by comparing the specific surface area of AC before and after loading $Mg(BH_4)_2{\cdot}6NH_3$. As shown in Table 1, the surface area measured by the BET method was dramatically reduced from 2051 $m^2\ g^{-1}$ to 621.1 $m^2\ g^{-1}$ after forming the 0.2:1 $Mg(BH_4)_2{\cdot}6NH_3$@AC nanocomposite. Further calculation revealed that the micropore volume was reduced from 0.835 $cm^3\ g^{-1}$ to 0.246 $cm^3\ g^{-1}$, which provide another strong piece of evidence for the successful nanoconfinement of $Mg(BH_4)_2{\cdot}6NH_3$ in AC.

Figure 3 presents the FTIR spectra of the as-prepared $Mg(BH_4)_2{\cdot}6NH_3$@AC nanocomposites. The bulk

Table 1. BET results of AC and PC before and after nanoconfinement

| | activated carbon (AC) | porous carbon (4 nm) | porous carbon (6 nm) | porous carbon (10 nm) |
|---|---|---|---|---|
| surface area (SBET, $m^2 g^{-1}$, pristine) | 2051 | 1034 | 222 | 105 |
| surface area (SBET, $m^2 g^{-1}$, nanoconfied) | 621 | 295 | 0 | 0 |
| micropore volume ($cm^3 g^{-1}$, pristine) | 0.835 | 0.426 | 0.093 | 0.05 |
| micropore volume ($cm^3 g^{-1}$, nanoconfined | 0.246 | 0.118 | 0 | 0 |

$Mg(BH_4)_2{\cdot}6NH_3$ synthesized by reacting $Mg(BH_4)_2{\cdot}2Et_2O$ with $NH_3$ shows the typical absorbances of the N-H vibrations (3360, 3266 and 3202 $cm^{-1}$) in the $NH_3$ group and the B-H vibrations (2293, 2248, 2161, 1203 and 1085 $cm^{-1}$), which are identical to the FTIR characteristics of $Mg(BH_4)_2{\cdot}6NH_3$ prepared by ball milling $Mg(BH_4)_2$ under $NH_3$ atmosphere.[37] After nanoconfinement, some appreciable changes were observed in the N-H and B-H vibrations. With increasing AC content, the relative intensity of the N-H absorbance at 3360 $cm^{-1}$ gradually decreased, whereas the absorption bands at 3266 and 3202 $cm^{-1}$ were intensified. In particular, a red shift was detected from 3266 and 3202 $cm^{-1}$ to 3251 and 3188 $cm^{-1}$ for the N-H absorbances for the 0.4:1 and 0.2:1 $Mg(BH_4)_2{\cdot}6NH_3$@AC nanocomposites, suggesting the weakening of the N-H bonding. On the contrary, a gradual blue shift occurred for the B-H vibration with increasing AC content in the $Mg(BH_4)_2{\cdot}6NH_3$@AC nanocomposites as the absorbances of the B-H vibration at 2294, 2248 and 2159 $cm^{-1}$ shifted to 2361, 2291 and 2225 $cm^{-1}$, respectively, representing a strengthening of the B-H bonding. These facts indicate that confining $Mg(BH_4)_2{\cdot}6NH_3$ in micropores of the AC changes the bonding nature of N-H and B-H bonds. This facilitates the improvement of the thermodynamic and/or kinetic properties of hydrogen release from $Mg(BH_4)_2{\cdot}6NH_3$.

### 3.2 Dehydrogenation Properties of Nanoconfined $Mg(BH_4)_2{\cdot}6NH_3$

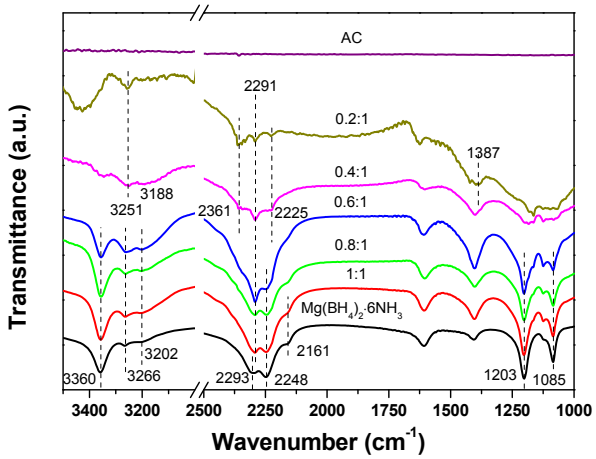


**Figure 3.** FTIR spectra of the commercial AC, bulk $Mg(BH_4)_2{\cdot}6NH_3$ and $Mg(BH_4)_2{\cdot}6NH_3$@AC nanocomposites.

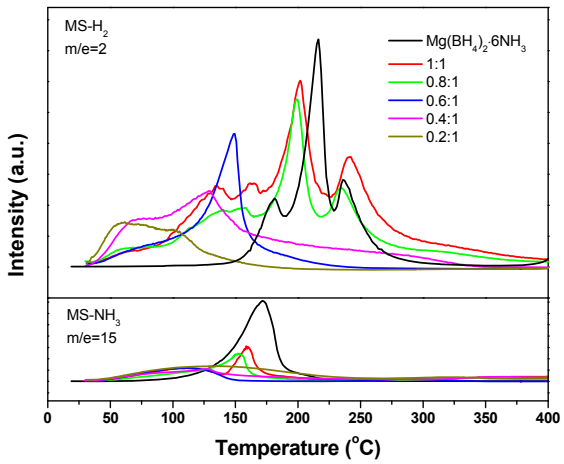


**Figure 4.** TPD-MS curves of the bulk $Mg(BH_4)_2{\cdot}6NH_3$ and as-prepared $Mg(BH_4)_2{\cdot}6NH_3$@AC nanocomposites.

The as-prepared $Mg(BH_4)_2{\cdot}6NH_3$@AC nanocomposites were then subjected to dehydrogenation as a function of temperature. Figure 4 shows the TPD-MS curves of the bulk $Mg(BH_4)_2{\cdot}6NH_3$ and the as-prepared $Mg(BH_4)_2{\cdot}6NH_3$@AC nanocomposites. It is apparent that the nanoconfinement changes the dehydrogenation behavior of the $Mg(BH_4)_2{\cdot}6NH_3$@AC. Upon heating, the bulk $Mg(BH_4)_2{\cdot}6NH_3$ started releasing hydrogen at approximately 125 ºC, and three distinct dehydrogenation peaks appeared at 197, 228 and 250 ºC. The hydrogen release from the $Mg(BH_4)_2{\cdot}6NH_3$ terminated at 350 ºC. Interestingly, the nanoconfined $Mg(BH_4)_2{\cdot}6NH_3$@AC exhibited very different dehydrogenation behaviors from its bulk counterpart, especially for the nanoconfined samples with higher AC contents. For the 1:1 $Mg(BH_4)_2{\cdot}6NH_3$@AC nanocomposite, the onset dehydrogenation temperature was lowered dramatically to only 40 ºC, which is 85 ºC lower than that of the bulk $Mg(BH_4)_2{\cdot}6NH_3$. However, the majority of dehydrogenation still occurred at 150-350 ºC. With increasing AC content, the onset dehydrogenation temperature remained almost constant, whereas the dehydrogenation peak moved to lower temperatures. The peak temperature of the 0.6:1 $Mg(BH_4)_2{\cdot}6NH_3$@AC nanocomposite was reduced to 148 ºC, and the terminal temperature for hydrogen desorption was lowered to 240 ºC. While the AC content was increased to 0.2:1, hydrogen desorption mainly occurred at 40-175 ºC with distinctly reduced peak intensities caused by the lower relative content of the $Mg(BH_4)_2{\cdot}6NH_3$ active species. The reduction of the operating temperature for dehydrogenation may be attributed to two factors: the nanosize effect and the interaction between $Mg(BH_4)_2{\cdot}6NH_3$ and carbon scaffolds. However, the $Mg(BH_4)_2{\cdot}6NH_3$@graphite composites prepared under the same conditions exhibit a nearly identical dehydrogenation behavior to that of the pristine $Mg(BH_4)_2{\cdot}6NH_3$ (Figure S5, ESI). That is, no apparent change in dehydrogenation behavior was observed after combining $Mg(BH_4)_2{\cdot}6NH_3$ and graphite. As graphite is a bulk material without porosity, it can be speculated that there is no interaction between $Mg(BH_4)_2{\cdot}6NH_3$ and carbon in this

system. We therefore believe that the reduction in the dehydrogenation temperature of the $Mg(BH_4)_2{\cdot}6NH_3$@AC nanocomposites should be mainly attributed to the nanosize effect caused by nanoconfinement.

In addition, it is noteworthy that the ammonia-release behaviors of $Mg(BH_4)_2{\cdot}6NH_3$ were also changed remarkably after confining it in the AC scaffold. As shown in Figure 4, a strong $NH_3$ peak was detected at 80-225 ºC for the pristine sample. However, the ammonia release from the $Mg(BH_4)_2{\cdot}6NH_3$@AC nanocomposites showed a wide peak with a low-temperature shift and significantly decreased intensity. The onset temperature for the ammonia release of the 0.2:1 $Mg(BH_4)_2{\cdot}6NH_3$@AC nanocomposite was approximately 50 ºC, slightly higher than that of dehydrogenation. This is quite different from the case of the pristine $Mg(BH_4)_2{\cdot}6NH_3$, in which ammonia was released prior to hydrogen. This difference suggests that the thermal decomposition pathway of $Mg(BH_4)_2{\cdot}6NH_3$ may be different after nanoconfinement.

Figure 5 presents the volumetric release curves of the bulk $Mg(BH_4)_2{\cdot}6NH_3$ and as-prepared $Mg(BH_4)_2{\cdot}6NH_3$@AC nanocomposites. Here, the gas-evolution amounts for the $Mg(BH_4)_2{\cdot}6NH_3$@AC nanocomposites have been corrected by excluding the contents of activated carbon. As shown in Figure 5, the bulk $Mg(BH_4)_2{\cdot}6NH_3$ began to sluggishly release gases at 80 ºC, and the gas release gradually accelerated at 125 ºC, which is consistent with the TPD-MS result. During heating up to 350 ºC, approximately 10.4 equiv. of gases was released from one mole of $Mg(BH_4)_2{\cdot}6NH_3$. As expected, the onset temperatures for gas evolution from $Mg(BH_4)_2{\cdot}6NH_3$ were significantly reduced to 40 ºC after confinement in the AC scaffold. Meanwhile, the majority of the dehydrogenation also shifted to lower temperatures, which is further confirmed by plotting the reaction extent against temperature (Figure 5b). It is observed that the 0.2:1 $Mg(BH_4)_2{\cdot}6NH_3$@AC nanocomposite released 59% of its hydrogen capacity at 150 ºC, compared to only 13% for the pristine sample. However, the total amounts of gas evolved decreased to 9.3, 8.8, 8.6, 8.1 and 6.3 equiv. for the 1:1, 0.8:1, 0.6:1, 0.4:1 and 0.2:1 $Mg(BH_4)_2{\cdot}6NH_3$@AC nanocomposites, respectively. Clearly, increases in the AC content decreased the amount of gas evolved from the nanocomposites. Further TG examination confirmed this conclusion (Figure S6, ESI). As mentioned above, the onset dehydrogenation temperature of $Mg(BH_4)_2{\cdot}6NH_3$@AC nanocomposites was reduced to only 40 ºC, and hydrogen release was initiated prior to ammonia evolution, as shown in Figure 4. In addition, it should be mentioned that the $Mg(BH_4)_2{\cdot}6NH_3$@AC nanocomposites were prepared in an ammonia atmosphere at 0 ºC. Thus, as the sample temperature was increased from 0 ºC to ambient temperature (~ 35 ºC) during the preparation process, some hydrogen may be liberated. The lack of hydrogen capacity loss for the $Mg(BH_4)_2{\cdot}6NH_3$@graphite composites (Figure S7, ESI) provides additional evidence for the occurrence of hydrogen desorption during the preparation of $Mg(BH_4)_2{\cdot}6NH_3$@AC nanocomposites.

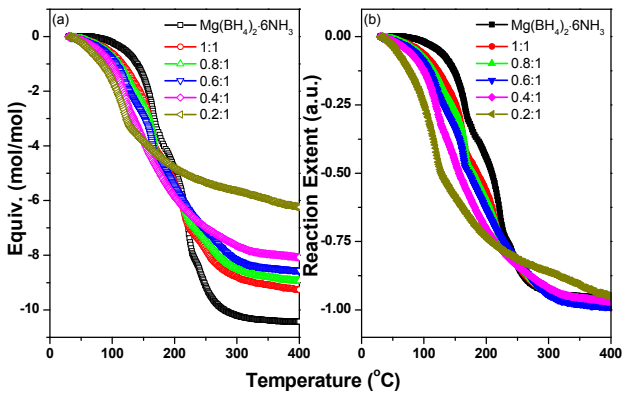


**Figure 5**. Volumetric release (a) and reaction extent (b) curves of the bulk $Mg(BH_4)_2{\cdot}6NH_3$ and $Mg(BH_4)_2{\cdot}6NH_3$@AC nanocomposites.

### 3.3 Thermodynamic Behaviors of Nanoconfined $Mg(BH_4)_2{\cdot}6NH_3$

To understand the effects of nanoconfinement on the thermodynamic properties of hydrogen desorption from $Mg(BH_4)_2{\cdot}6NH_3$, DSC measurements were conducted on the as-prepared $Mg(BH_4)_2{\cdot}6NH_3$@AC nanocomposites with a heating rate of 10 ºC $min^{-1}$. The results are displayed in Figure 6. Here, it should be noted that the DSC data were corrected by excluding the AC content. As reported in our previous work,[37] three thermal events were detected for the bulk $Mg(BH_4)_2{\cdot}6NH_3$ upon heating. A strong endothermic peak at 202 ºC originating from the deammoniation reaction was followed by an exothermic peak and a weak endothermic peak. The exothermic event was attributed to the dehydrogenation reaction of $Mg(BH_4)_2{\cdot}6NH_3$ driven by the local $H^{\delta+}$-$H^{\delta-}$ combination, which gives rise to the formation of thermodynamically stable B-N bonds. Such exothermic effects of hydrogen release make reversible hydrogen storage in $Mg(BH_4)_2{\cdot}6NH_3$ quite difficult. After nanoconfinement, the initial endothermic peaks at 202 and 272 ºC and exothermic peak at 250 ºC gradually shifted to lower temperatures and decreased dramatically in intensity with increasing AC content.

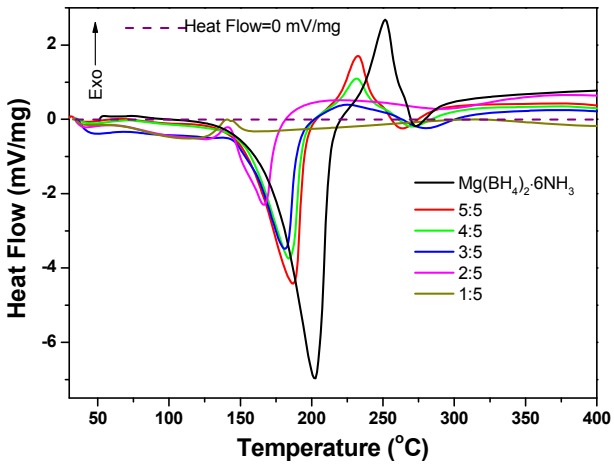


**Figure 6**. DSC curves of the bulk $Mg(BH_4)_2{\cdot}6NH_3$ and $Mg(BH_4)_2{\cdot}6NH_3$@AC nanocomposites.

In particular, a new broad endothermic peak emerged at 35-140 ºC for a $Mg(BH_4)_2$:AC weight ratio of less than 0.6:1. Meanwhile, the exothermic peak shifted to 225 ºC and markedly decreased in intensity. More interestingly, only two broad endothermic peaks were observed at 35-140 ºC and 140-280 ºC for the 0.2:1 $Mg(BH_4)_2·6NH_3$@AC nanocomposite, and the exothermic peak was invisible, experimentally indicating a change in the dehydrogenation thermodynamics. On the contrary, no appreciable change was detected for the $Mg(BH_4)_2·6NH_3$@graphite composites except for the slightly reduced peak intensities (Figure S8, ESI), which provides additional evidence for the nanoconfinement-induced thermodynamic improvement of hydrogen desorption from $Mg(BH_4)_2·6NH_3$@AC nanocomposites.

To further clarify how particle size affects the thermodynamic properties of $Mg(BH_4)_2·6NH_3$, porous carbon (PC) with different pore sizes of 4 nm, 6 nm and 10 nm was further used as the carbon scaffolds. Three $Mg(BH_4)_2·6NH_3$@PC nanocomposites with a starting weight ratio of 0.2:1 for $Mg(BH_4)_2$ and PC were prepared by the same procedure as the $Mg(BH_4)_2·6NH_3$@AC nanocomposites. In addition, the 0.2:1 $Mg(BH_4)_2·6NH_3$@AC nanocomposite was denoted as the 2-nm sample because the pore size of AC is approximately 2 nm. XRD analyses of these samples revealed a pore-size dependence of the crystallinity of $Mg(BH_4)_2·6NH_3$. As shown in Figure 7, the diffraction peaks of $Mg(BH_4)_2·6NH_3$ were gradually weakened with decreasing pore size and even disappeared completely when the pore size was reduced to 2 nm, indicating a poor crystallinity caused by nanoconfinement. The detection of very weak diffraction peaks from $Mg(BH_4)_2·6NH_3$ in the three $Mg(BH_4)_2·6NH_3$@PC samples should be attributed to the lower micropore volumes (0.426, 0.093 and 0.050 $cm^3\ g^{-1}$ for the 4 nm-, 6 nm- and 10 nm PC, respectively, in comparison with 0.8353 $cm^3\ g^{-1}$ for AC) and/or larger pores of porous carbons relative to AC. This fact also suggests that $Mg(BH_4)_2·6NH_3$ was indeed confined in the micropores of PC and AC.

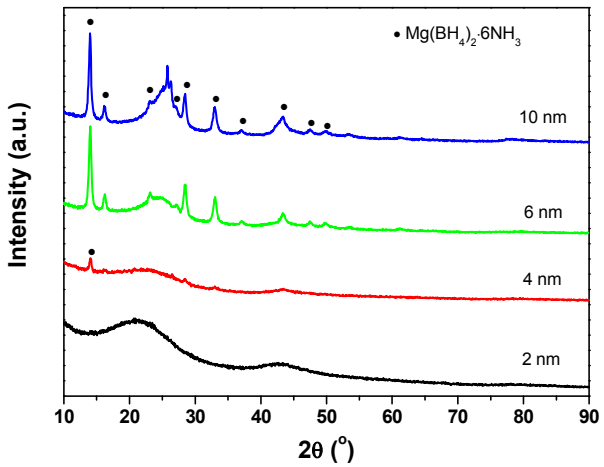


**Figure 7**. XRD patterns of $Mg(BH_4)_2·6NH_3$@AC and $Mg(BH_4)_2·6NH_3$@PC with different pore sizes.

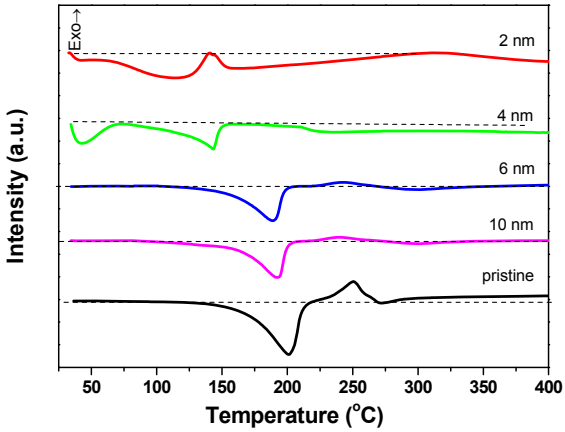


**Figure 8**. DSC curves of the bulk $Mg(BH_4)_2·6NH_3$, $Mg(BH_4)_2·6NH_3$@AC and $Mg(BH_4)_2·6NH_4$@PC nanocomposites.

Figure 8 shows the DSC curves of the $Mg(BH_4)_2·6NH_3$@PC and $Mg(BH_4)_2·6NH_3$@AC nanocomposites. With decreasing pore size of carbon scaffolds, the endothermic event at 202 ºC shifted to lower temperatures, and the peak intensity of the exothermic event at 250 ºC decreased dramatically. For the 4-nm carbon scaffold, the exothermic peak at 250 ºC was absent, and a new endothermic peak was detected at 35-70 ºC with a low-temperature shift to 144 ºC for the main endothermic peak. Specifically, reducing the particle size of $Mg(BH_4)_2·6NH_3$ is quite effective for tuning its decomposition thermodynamic behaviors due to its significantly increased surface energy and the excess enthalpy and strains at the grain boundaries. In addition, 4 nm is found to be the critical size for the transition of the heat effect from exothermic to endothermic in the present study. Further TPD-MS measurements revealed that the endothermic events in the 4-nm sample should mainly correspond to hydrogen release (Figure S9, ESI).

### 3.4 Dehydrogenation Mechanisms of Nanoconfined $Mg(BH_4)_2·6NH_3$

To further understand the dehydrogenation mechanisms of nanoconfined $Mg(BH_4)_2·6NH_3$, the thermal decomposition products of the 0.2:1 $Mg(BH_4)_2·6NH_3$@AC nanocomposite were collected and subjected to XRD and FTIR analyses. The results are presented in Figure 9. In our previous work,[37] it was revealed that the final decomposition product of bulk $Mg(BH_4)_2·6NH_3$ was composed mainly of metallic Mg and BN. For the 0.2:1 $Mg(BH_4)_2·6NH_3$@AC nanocomposite, however, the decomposition product exhibits identical XRD characteristics to the as-prepared sample, namely, only two broad peaks at 15-30º and 40-50º from AC were detected. The typical diffraction peaks of metallic Mg, which is usually well crystallized under the experimental conditions, were not observed, suggesting the formation of a new Mg-based amorphous compound. As shown in Figure 9b, some discrepancies were also found in the FTIR spectrum of the dehydrogenated $Mg(BH_4)_2·6NH_3$@AC nanocomposite with respect to that of the decomposed bulk sample. The B-N absorption bands at 1380 and 1148 $cm^{-1}$ moved to 1400 and

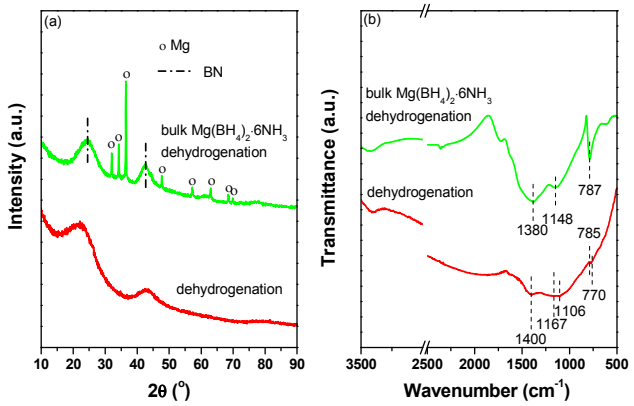


**Figure 9**. XRD patterns (a) and FTIR spectra (b) of the decomposed bulk $Mg(BH_4)_2·6NH_3$ and 0.2:1 $Mg(BH_4)_2·6NH_3$@AC nanocomposite.

1167 $cm^{-1}$, respectively; that is, a blue shift occurred. In contrast, a red shift was observed from 787 to 785 $cm^{-1}$. At the same time, two new B-N absorption bands at 1106 and 770 $cm^{-1}$ also emerged in the FTIR spectrum. These facts reveal that new compounds containing B-N bonds were produced after the decomposition of the $Mg(BH_4)_2·6NH_3$@AC nanocomposite.

Further XPS measurements were conducted on the dehydrogenated 0.2:1 $Mg(BH_4)_2·6NH_3$@AC nanocomposite to characterize the chemical states of Mg, B and N. Figure 10 presents the high-resolution spectra of Mg 1s, B 1s and N 1s. It is observed that the Mg 1s spectrum could be resolved into two signals at 1304.6 and 1305.3 eV by peak fitting. These signals are different from the characteristic XPS peaks of metallic Mg, one of the decomposition products of bulk $Mg(BH_4)_2·6NH_3$,[38] and $MgB_2$, a decomposition product of $Mg(BH_4)_2$.[39] This result further suggests the possible existence of new Mg-containing compounds. As for the B 1s spectrum, the signal was fitted with two peaks at 192.0 and 190.7 eV. The peak at 192.0 eV was attributed to the signal of amorphous BN with N/B<1,[40] and

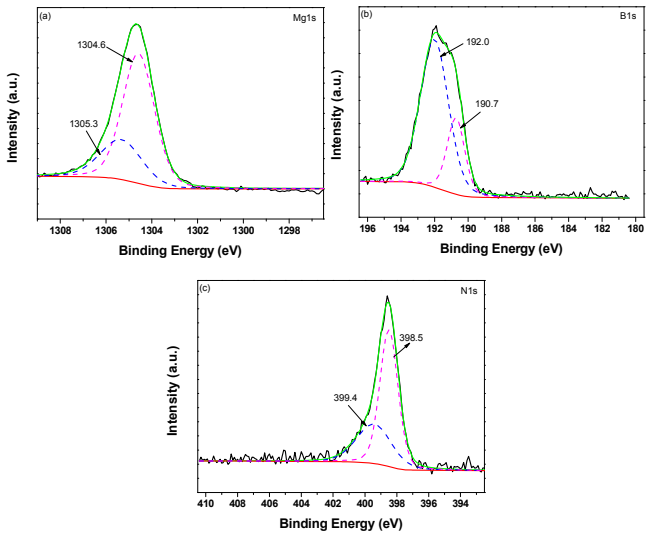


**Figure 10**. High-resolution Mg 1s (a), B 1s (b) and N 1s (c) spectra of the fully decomposed 0.2:1 $Mg(BH_4)_2·6NH_3$@AC nanocomposite.

that at 190.7 eV was assigned to other B-containing compounds. The N 1s peak is also composed of two peaks at 398.5 and 399.4 eV. Of these peaks, that at 398.5 eV was ascribed to amorphous BN,[40] and that at 399.4 eV might originate from a new N-containing compound. We therefore believe that after the dehydrogenation of the 0.2:1 $Mg(BH_4)_2·6NH_3$@AC nanocomposite, a new Mg-B-N compound may be formed in addition to the amorphous BN. In other words, the decomposition product of the 0.2:1 $Mg(BH_4)_2·6NH_3$@AC nanocomposite should mainly consist of amorphous BN and a new Mg-B-N compound. When $Mg(BH_4)_2·6NH_3$ was confined in micropores, the surrounding pore wall forced all of the elements (Mg, B and N) to stay in close vicinity. In addition, the nanosized particles possessed higher chemical activity. All of these factors favor the combination of Mg, B and N, which induces the formation of a novel Mg-B-N compound during the decomposition of nanoconfined $Mg(BH_4)_2·6NH_3$ instead of metallic Mg. As mentioned above, the N/B atomic ratio of BN in this case is less than 1; accordingly, the N/B atomic ratio in the newly developed Mg-B-N compound should be greater than 1, which is consistent with the well-known $Mg_3BN_3$ and $Mg_3B_2N_4$.

According to the above discussions, the dehydrogenation thermodynamics of $Mg(BH_4)_2·6NH_3$ were effectively tuned to be of endothermic nature through nanoconfinement associated with significantly reduced operating temperatures. It is well known that, in bulk $Mg(BH_4)_2·6NH_3$, the Mg-N bond is first broken with ammonia release upon heating. However, after nanoconfinement, the crystal structure of $Mg(BH_4)_2·6NH_3$ was disrupted, exposing a large number of high-energy surfaces with active $[BH_4]^-$ anions and $NH_3$ groups. The local combination of $H^{\delta+}$ in $NH_3$ groups and $H^{\delta-}$ in $[BH_4]^-$ anions on these high-energy surfaces is much more favorable, resulting in a low onset dehydrogenation temperature of 40 ºC. In addition, the decomposition product of the nanoconfined $Mg(BH_4)_2·6NH_3$ is composed of BN and a Mg-B-N compound due to the intact contact of Mg, B and N caused by the enwrapping effect of the surrounding pore walls and the higher chemical activities of nanosized materials relative to metallic Mg and BN for the bulk $Mg(BH_4)_2·6NH_3$ as mentioned above, which should be the primary contributors to the tailoring of the thermodynamics. Meanwhile, from a kinetic point of view, the significantly shortened diffusion distance and increased number of reaction sites on AC distinctly enhanced the dehydrogenation kinetics of nanoconfined $Mg(BH_4)_4·6NH_3$, thus also contributing to the improved dehydrogenation properties.

### 3.5 Hydrogenation of the Dehydrogenated $Mg(BH_4)_2·6NH_3$@AC Nanocomposite

As mentioned above, the dehydrogenation of the nanoconfined $Mg(BH_4)_2·6NH_3$ was modified to be endothermic in nature, satisfying the thermodynamic needs of reversible hydrogen storage. Therefore, to evaluate the hydrogen storage reversibility of nanoconfined $Mg(BH_4)_2·6NH_3$, the dehydrogenated 0.2:1 $Mg(BH_4)_2·6NH_3$@AC nanocomposite was re-hydrogenated at 400 ºC and an initial hydrogen pressure

of 100 bar. Unfortunately, no hydrogen uptake was detected, possibly due to the insufficient hydrogenation conditions. Therefore, further investigations on the kinetic destabilization in the nanoconfined $Mg(BH_4)_2{\cdot}6NH_3$ should be conducted to achieve reversible hydrogen storage.

## Conclusions

This work demonstrates that reducing the particle sizes significantly improved the dehydrogenation thermodynamics of $Mg(BH_4)_2{\cdot}6NH_3$, lowered the dehydrogenation operating temperature and reduced the evolution of $NH_3$. The 0.2:1 $Mg(BH_4)_2{\cdot}6NH_3$@AC nanocomposite began to release hydrogen at approximately 40 ºC, which is 85 ºC lower than the bulk $Mg(BH_4)_2{\cdot}6NH_3$. Upon heating to 150 ºC, a reaction extent of more than 59% for hydrogen release from the nanoconfined $Mg(BH_4)_2{\cdot}6NH_3$ was achieved, compared to only 13% for the bulk $Mg(BH_4)_2{\cdot}6NH_3$. In particular, the nanoconfined $Mg(BH_4)_2{\cdot}6NH_3$ exhibited an endothermic dehydrogenation behavior, which has not been observed for the metal borohydride ammoniates in previous reports. Mechanistic investigations revealed that the decomposition pathway of the nanoconfined $Mg(BH_4)_2{\cdot}6NH_3$ was altered, as BN and a novel Mg-B-N compound were formed as the products instead of Mg and BN. This phenomenon was mainly attributed to the nanoconfinement effect of the carbon scaffolds. Unfortunately, an attempt to hydrogenate the fully dehydrogenated $Mg(BH_4)_2{\cdot}6NH_3$@AC nanocomposite failed, possibly due to the higher kinetic barrier.

## Acknowledgements

We gratefully acknowledge financial support received from the National Natural Science Foundation of China (51171170, 51222101), the Research Fund for the Doctoral Program of Higher Education of China (20130101110080, 20130101130007), the Program for Innovative Research Team in University of Ministry of Education of China (IRT13037), and the Fundamental Research Funds for the Central Universities (2014XZZX003-08).

## Notes

[a]State Key Laboratory of Silicon Materials, Key Laboratory of Advanced Materials and Applications for Batteries of Zhejiang Province and School of Materials Science and Engineering, Zhejiang University, Hangzhou 310027, China
[b]Xi'an Modern Chemistry Research Institute, Xi'an 710065, China

†Electronic Supplementary Information (ESI) available: SEM of AC, graphite and $Mg(BH_4)_2{\cdot}6NH_3$@AC, XRD of $Mg(BH_4)_2{\cdot}6NH_3$, graphite and $Mg(BH_4)_2{\cdot}6NH_3$@graphite, MS and TG of $Mg(BH_4)_2{\cdot}6NH_3$@AC, MS of $Mg(BH_4)_2{\cdot}6NH_3$@PC, Volumetric release and DSC of $Mg(BH_4)_2{\cdot}6NH_3$@graphite, Microstructural characteristics of AC and PC. See DOI: 10.1039/b000000x/

## References

1 L. Schlapbach, A. Züttel, *Nature*, 2001, **414**, 353.
2 P. Chen, M. Zhu, *Mater. Today*, 2008, **11**, 36.
3 M. B. Ley, L. H. Jepsen, Y. -S. Lee, Y. W. Cho, J. M. B. von Colbe, M. Dornheim, M. Rokni, J. O. Jensen, M. Sloth, Y. Filinchuk, J. E. Jørgensen, F. Besenbacher and T. R. Jensen, *Mater. Today*, 2014, **17**, 122.
4 H.-W. Li, Y. Yan, S.-i. Orimo, A. Züttel and C. M. Jensen, *Energies*, 2011, **4**, 185.
5 *Targets for Onboard Hydrogen Storage Sytestem for Light-Duty Vehicles(2009)*. http://energy.gov/eere/fuelcells/downloads/targets-onboard-hydrogen-storage-systems-light-duty-vehicles. Accessed 10 October 2009.
6 N. Hanada, K. Chłopek, C. Frommen, W. Lohstroh and M. Fichtner, *J. Mater. Chem.*, 2008, **18**, 2611.
7 P. Chen, Z. Xiong, J. Luo, J. Lin and K. L. Tan, *Nature*, 2002, **420**, 302.
8 G. Soloveichik, J. -H. Her, P. W. Stephens, Y. Gao, J. Rijssenbeek, M. Andrus and J.-C. Zhao, *Inorg. Chem.*, 2008, **47**, 4290.
9 S. R. Johnson, W. I. David, D. M. Royse, M. Sommariva, C. Y. Tang, F. Fabbiani, M. O. Jones and P. P. Edwards, *Chem. Asian J.*, 2009, **4**, 849.
10 Y. J. Yang, Y. F. Liu, Y. Li, M. X. Gao and H. G. Pan, *Chem. Asian J.*, 2013, **8**, 476.
11 H. Chu, G. Wu, Z. Xiong, J. Guo, T. He and P. Chen, *Chem. Mater.,* 2010, **22**, 6021.
12 Y. Guo, X. Yu, W. Sun, D. Sun and W. Yang, *Angew. Chem. Int. Ed.*, 2011, **50**, 1087.
13 Y. J. Yang, Y. F. Liu, H. Wu, W. Zhou, M. X. Gao and H. G. Pan, *Phys. Chem. Chem. Phys.*, 2014, **16**, 135.
14 Y. Guo, H. Wu, W. Zhou and X. Yu, *J. Am. Chem. Soc.*, 2011, **133**, 4690.
15 F. Yuan, Q. Gu, X. Chen, Y. Tan, Y. Guo and X. Yu, *Chem. Mater.*, 2012, **24**, 3370.
16 J. J. Vajo, S. L. Skeith and F. Mertens, *J. Phys. Chem. B*, 2005, **109**, 3719.
17 H. W. Brinks, A. Fossdal, B. C. Hauback, *J. Phys. Chem. C*, 2008, **112**, 5658.
18 L. Mosegaard, B. Møller, J. -E. Jørgensen, Y. Filinchuk, Y. Cerenius, J. Hanson, E. Dimasi, F. Besenbacher and T. Jensen, *J. Phys. Chem. C*, 2008, **112**, 1299.
19 E. A. Nickels, M. O. Jones, W. I. F. David, S. R. Johnson, R. L. Lowton, M. Sommariva and P. P. Edwards, *Angew. Chem. Int. Ed.*, 2008, **47**, 2817.
20 Y. S. Chua, W. Li, G. Wu, Z. Xiong, P. Chen, *Chem. Mater.*, 2012, **24**, 3574.
21 Y. F. Zhou, Y. F. Liu, W. Wu, Y. Zhang, M. X. Gao and H. G. Pan, *J. Phys. Chem. C*, 2012, **116**, 1588.
22 P. A. Anderson, P. A. Chater, D. R. Hewett and P. R. Slater, *Faraday Discuss.*, 2011, **151**, 271.
23 Y. P. Pang, Y. F. Liu, M. X. Gao, L. Z. Ouyang, J. W. Liu, H. Wang, M. Zhu and H. G. Pan, *Nat. Commun.* 2014, **5**, 3519.
24 P. E. de Jongh, M. Alledort, J. J. Vajo and C. Zlotea, *MRS Bull.* 2013, **3**, 488.
25 P. E. de Jongh and P. Adelhelm, *ChemSusChem*, 2010, **3**, 1332.
26 A. Gutowska, L. Li, Y. Shin, C. M. Wang, X. S. Li, J. C. Linehan, R. S. Smith, B. D. Kay, B. Schmid and W. Shaw, *Angew. Chem. Int. Ed.*, 2005, **44**, 3578.

27 S. Zheng, F. Fang, G. Zhou, G. Chen, L. Ouyang, M. Zhu and D. Sun, *Chem. Mater.* 2008, **20**, 3954.
28 J. Gao, P. Adelhelm, M. H. Verkuijlen, C. Rongeat, M. Herrich, P. J. M. van Bentum, O. Gutfleisch, A. P. Kentgens, K. P. de Jong and P. E. de Jongh, *J. Phys. Chem. C*, 2010, **114**, 4675.
29 W. Lohstroh, A. Roth, H. Hahn and M. Fichtner, *ChemPhysChem*, 2010, **11**, 789.
30 S. Cahen, J. -B. Eymery, R. Janot and J. -M. Tarascon, *J. Power Source*, 2009, **189**, 902.
31 Z. Z. Fang, P. Wang, T. E. Rufford, X. D. Kang, G. Q. Lu and H. M. Cheng, *Acta Mater.*, 2008, **56**, 6257.
32 P. Ngene, R. van den Berg, M. H. Verkuijlen, K. P. de Jong and P. E. de Jongh, *Energy Environ. Sci.*, 2011, **4**, 4108.
33 Z. Zhao-Karger, R. Witter, E. G. Bardají, D. Wang, D. Cossement and M. Fichtner, *J. Mater. Chem. A*, 2013, **1**, 3379.
34 H. Wu, W. Zhou, K. Wang, T. J. Udovic, J. J. Rush, T. Yildirim, L. A. Bendersky, A. F. Gross, S. L. Van Atta, J. J. Vajo, F. E. Pinkerton and M. S. Meyer, *Nanotechnology*, 2009, **20**, 204002.
35 S. Li, W. Sun, Z. Tang, Y. Guo and X. Yu, *Int. J. Hydrogen Energy*, 2012, **37**, 3328.
36 Y. J. Yang, M. X. Gao, Y. F. Liu, J. H. Wang, J. Gu, H. G. Pan and Z. X. Guo, *Int. J. Hydrogen Energy*, 2012, **37**, 10733.
37 Y. J. Yang, Y. F. Liu, Y. Li, M. X. Gao and H. G. Pan, *J. Phys. Chem. C*, 2013, **117**, 16326.
38 K. Yates and R. West, *Surf. Interface Anal.*, 1983, **5**, 133.
39 K. Prince, V. Feyer, A. Tadich, L. Thomsen and B. Cowie, *J. Phys.: Condens. Matter.*, 2009, **21**, 405701.
40 C. Guimon, D. Gonbeau, G. Pfister-Guillouzo, O. Dugne, A. Guette, R. Naslain and M. Lahaye, *Surf. Interface Anal.*, 1990, **16**, 440.

## Graphical contents entry:

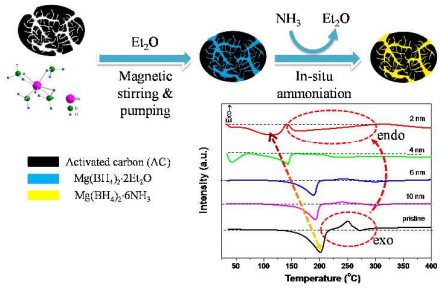


An endothermic dehydrogenation is achieved for $Mg(BH_4)_2 \bullet 6NH_3$ confined in porous scaffolds with less than 4 nm of pore size.